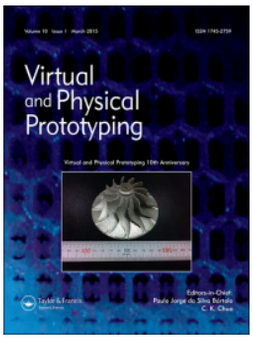

Virtual and Physical Prototyping

ISSN: (Print) (Online) Journal homepage: www.tandfonline.com/journals/nvpp20

Effect of hot isostatic pressing on porosity of wire-arc directed energy deposited TZM/NbZr1 bimetallic structure

Gazi Tanvir, Md Abdul Karim, Sainand Jadhav, Saiful Islam, Young-Min Kim, Ho Jin Ryu & Duck Bong Kim

To cite this article: Gazi Tanvir, Md Abdul Karim, Sainand Jadhav, Saiful Islam, Young-Min Kim, Ho Jin Ryu & Duck Bong Kim (2024) Effect of hot isostatic pressing on porosity of wire-arc directed energy deposited TZM/NbZr1 bimetallic structure, Virtual and Physical Prototyping, 19:1, e2404989, DOI: 10.1080/17452759.2024.2404989

To link to this article: https://doi.org/10.1080/17452759.2024.2404989

Published online: 24 Sep 2024.

VIRTUAL AND PHYSICAL PROTOTYPING
2024, VOL. 19, NO. 1, e2404989 (20 pages)
https://doi.org/10.1080/17452759.2024.2404989

Taylor & Francis
Taylor & Francis Group

Effect of hot isostatic pressing on porosity of wire-arc directed energy deposited TZM/NbZr1 bimetallic structure

Gazi Tanvir[a], Md Abdul Karim[a], Sainand Jadhav[a], Saiful Islam[a], Young-Min Kim[b], Ho Jin Ryu[c,d] and Duck Bong Kim[e]

[a]Department of Mechanical Engineering, Tennessee Technological University, Cookeville, TN, USA; [b]Advanced Joining & Additive Manufacturing R&D, Korea Institute of Industrial Technology (KITECH), Incheon Metropolitan City, Korea; [c]Department of Nuclear and Quantum Engineering, Korea Advanced Institute of Science and Technology, Daejeon, Korea; [d]Department of Material Science and Engineering, Korea Advanced Institute of Science and Technology, Daejeon, Korea; [e]Department of Manufacturing and Engineering Technology, Tennessee Technological University, Cookeville, TN, USA

ABSTRACT

This study evaluates the effectiveness of hot isostatic pressing (HIP) in mitigating porosity in TZM-NbZr1 bimetallic structures fabricated via wire-arc directed energy deposition (DED). Two distinct HIP conditions and a combined HIP and heat treatment (HT) were investigated. The pore area fraction decreased from $4 \pm 0.05\%$ in the as-built condition to $3.05 \pm 0.02\%$ and $1 \pm 0.01\%$ after treatment at 1200°C and 1500°C, respectively. Porosity was further reduced to $0.01 \pm 0.005\%$ with HIP at 1800°C followed by HT. Plastic deformation strongly influenced pore size and shape at elevated temperatures, particularly above the recrystallisation temperatures of both alloys. At lower treatment temperature, disparity in material flow around the pores resulted in interconnected micro-cracks or micro-void formation. However, the combined HIP and HT process effectively eliminated both cracks and porosities from the interface altering the pore recovery mechanism from micro-void formation to dynamic recrystallisation. Additionally, enhanced Mo diffusion from TZM to NbZr1 was observed at higher temperature.

ARTICLE HISTORY
Received 13 July 2024
Accepted 11 September 2024

KEYWORDS
Wire-arc additive manufacturing; hot isostatic pressing; heat treatment; pore recovery; bimetallic structure; refractory alloys

1. Introduction

Refractory alloys, renowned for their exceptional heat resistance, are essential in high-temperature applications [1]. The strategic use of multi-material structures composed of various refractory alloys is critical for meeting location-specific demands in such applications. For example, NbZr1 (Nb-1wt.% Zr) is a popular Nb-based low-density engineering material with superior ductility, stability against irradiation, and high-temperature strength compared to other refractory metals [2]. Titanium-Zirconium-Molybdenum (TZM), on the other hand, is a Mo-based structural material widely used in aerospace and nuclear industries, valued for its excellent thermo-physical properties at elevated temperatures and pressures, such as a low coefficient of thermal expansion (CTE), high thermal conductivity, enhanced mechanical properties, and exceptional creep resistance [3]. A bimetallic structure (BS) combining TZM and NbZr1 could, therefore, offer significant advantages in extreme conditions by leveraging the complementary properties of both alloys. However, there are several potential challenges in joining these two alloys. For instance, the absence of a solid solution between Mo and Nb below 2400°C in the Mo-Nb binary phase diagram indicates limited solubility between them [4]. Moreover, the mismatch in CTE between these two materials can lead to residual stresses in the fabricated structure [5].

Previous researches have explored different traditional bonding techniques to fabricate BS using TZM and NbZr1 which includes diffusion bonding [6], liquid metallic film bonding [7], and contact brazing [5]. Compared to conventional processes, additive manufacturing (AM) stands as a remarkable leap forward in producing multi-material structures. This innovative technology seamlessly integrates the advantages of different material combinations, unlocking unprecedented possibilities for producing intricate, lightweight, and high-performance components [8]. In this regard, the wire-arc directed energy deposition (DED) process, also known as wire-arc additive manufacturing (WAAM), provides several benefits among other metal

CONTACT Ho Jin Ryu hojinryu@kaist.ac.kr; Duck Bong Kim dkim@tntech.edu

additive manufacturing techniques. WAAM offers advantages such as a higher deposition rate, lower setup costs, operational simplicity, and enhanced energy efficiency compared to powder-bed or powder-fed processes [8–10]. These qualities could position WAAM as a preferred method for BS fabrication from refractory alloys like TZM and NbZr1.

However, the WAAM process introduces several challenges, including process optimisation, defect control, and maintaining structural homogeneity, which can limit the production of high-quality components [11, 12]. Various types of defects in the fabricated components can arise due to suboptimal process parameters, improper welding speed, contaminated wire feedstock, and inadequate shielding of the melt pool during deposition. In a study by Jadav et al. [13], the feasibility of a TZM/NbZr1 BS was investigated under different heat input conditions using WAAM. Despite achieving good interfacial bonding with high heat input, the microstructure at the TZM/NbZr1 interface exhibited multi-scale pores and solidification cracks. Gas porosities at the interface can be induced by the high-temperature oxygen affinity of Mo [14]. At temperature above 650°C, Mo forms an oxide layer of MoO_3, which has a boiling point significantly lower than the melting points of TZM and NbZr1. Consequently, during NbZr1 deposition (which melts at 2477°C) on TZM, MoO_3 can form in the presence of oxygen, resulting in gas porosity at the bimetal interface. In a study by Islam et al. [3], different types of porosity with similar pore formation mechanisms were identified in TZM alloy components fabricated using the WAAM process. These porosities were classified as small spherical pores (SSPs), inverse pear-shaped pores (IPPs), and large pores. Although these porosities only occupied a small fraction inside the manufactured components, their influence on the overall performance was crucial. Porosity decreases the part density, and it can also act as a crack initiation point, leading to premature failure and reduced mechanical properties [5, 14]. Therefore, minimising porosity and increasing part density is crucial for improving the strength and performance of the manufactured bimetallic structures.

Hot isostatic pressing (HIP) is one of the most popular techniques for porosity removal. Components produced through various AM techniques have recently undergone post-processing with HIP treatment, which promotes microstructural homogeneity and reduces anisotropy in the structure [15–20]. However, few studies have focused on the effect of HIP on bimetal structures, particularly in improving interfacial microstructure. For example, Polozov et al. investigated the effect of annealing and HIP on the Ti6Al-4 V/Ti2AlNb BS produced with selective laser melting (SLM) and studied the microstructural evolution at the interface [21]. They found that HIP treatment smoothed the transition of Nb content across the interface, primarily due to the decomposition of the α′-phase into α- and β-phases. In addition to eliminating residual porosity, HIP also mitigated a steep microhardness gradient between the two alloys, resulting in a more uniform microstructure along the transition zone. In another study by Terrazas et al., HIP was applied to a Ti64/Cu structure fabricated using the electron beam melting (EBM) process [22]. HIP treatment led to a significant increase in the width of the α phase due to coarsening at elevated temperatures and pressures. Additionally, an annealing twin was observed on the copper side, attributed to recrystallisation and grain growth during HIP. The copper side also exhibited a transition from an equiaxed to a columnar grain structure, moving away from the interface. These results highlight the complexity of successfully integrating HIP into bimetallic structures to improve interfacial microstructures, which poses greater challenges compared to its use on monolithic materials. In addition to HIP, heat treatment following HIP is frequently used to relieve residual stresses, refine microstructure, and homogenise the material. Furthermore, integrating HIP and heat treatment in the same equipment can result in increased efficiency by streamlining the processing steps, and reducing overall production costs [23]. For instance, Hafenstein et al. and Chadha et al. demonstrated that integrating HIP and heat treatment improved microstructural homogeneity in A356 cast alloy and 316L stainless steel, compared to conventional HIP alone [24, 25]. This integrated approach can similarly benefit the interfacial microstructure of refractory-based bimetallic structures.

While several studies reported the application of HIP treatment to minimise the porosity of various BS components, the current understanding of porosity reduction and its underlying mechanism in Mo-Nb based alloys remains inconclusive. Moreover, the existing literature offers limited exploration of HIP parameters at high temperatures, particularly above 1700°C. Chen et al. investigated the effect of high temperature-high pressure (1800°C, 180 MPa) HIP parameters to increase the thermal conductivity of laser-powder bed fusion produced pure tungsten [26]. However, the effectiveness of such high-temperature HIP conditions in reducing porosity in bimetallic structures and the resulting changes in interfacial microstructure have not been thoroughly explored. A comprehensive understanding of how bimetallic interfaces behave under these HIP conditions, and the subsequent microstructural changes, is crucial for improving material

properties and enhancing performance. This study investigates the effectiveness of various HIP treatments, including an integrated HIP and heat treatment process, in minimising porosity in WAAM-fabricated bimetallic structures of Mo-Nb based refractory alloys (TZM/NbZr1). Additionally, it examines the effects of these post-treatments on the bimetal interface, assessing changes in interfacial microstructure and elucidating the underlying pore recovery mechanisms. The findings from this research could offer valuable insights into optimising porosity levels at the bimetal interface of Mo-Nb based alloys produced by wire-based directed energy deposition (DED) techniques, thereby enhancing their suitability for demanding applications.

2 . Materials and methods

2.1. Thin wall deposition

In this experiment, a gas tungsten arc welding (GTAW)-based DED system was employed, comprising of a 6-axis Fanuc ArcMate 120iC robot arm with a Fanuc R-J3iB controller, a Miller Dynasty 400 power source, and a generic wire feeder. The robot, wire feeder, and power supply were instrumental in controlling the travel speed (TS), wire feed speed (WFS), and welding current, respectively. Details of the experimental setup can be found in a previous study by Jadav et al. [13].

To ensure uniformity, a consistent 5 mm gap between the electrode tip and the workpiece was maintained for each experiment, determining the welding voltage. Consumable NbZr1 (ASTM-B392) wire with a diameter of 0.95 mm was deposited on a TZM substrate having the dimension of 100 mm × 20 mm × 5 mm. Table 1 displays the elemental composition of TZM substrate and NbZr1 wire used in this study. An intermittent temperature of 200°C ± 10°C, known as the interpass temperature, was maintained after each layer of NbZr1 deposition, and the temperature was measured using a handheld K-type thermocouple. Two thin walls, each with identical heat input conditions, were deposited with the dimensions measured as 100 mm in length, 6–7 mm in width, and 35–36 mm in height. Figure 1 depicts one of the resulting thin walls of the TZM/NbZr1 bimetallic system, while Table 2 provides an overview of the process parameters employed in depositing these structures.

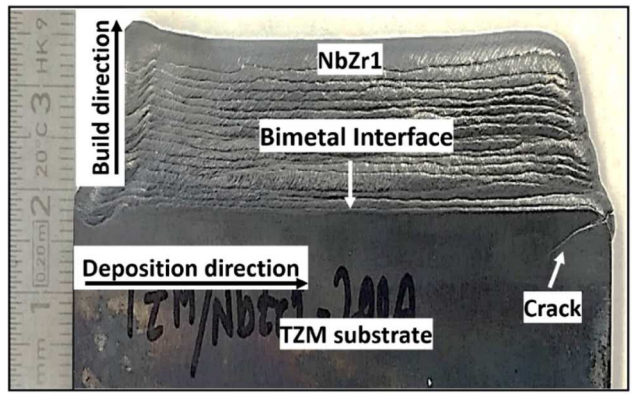

Figure 1. Wire-arc additively manufactured TZM/NbZr1 bimetallic thin-wall structure; NbZr1 wire was melted and deposited over TZM substrate. Deposition direction and building direction is also indicated with black arrow. A small edge crack is shown in white arrows which formed after the solidification of the final (top-most) layer.

Table 2. Process parameters used for NbZr1 deposition on TZM substrate.

Process parameters	Value
Diameter of the electrode	4 mm
Torch to wire feed angle	45
Torch Angle	90
Torch travel speed	20 cm/min
Wire feed speed	150 cm/min
Current	200A
Shielding gas flow rate	15 L/min
Shielding gas	99.999% Ar

2.2. Selecting HIP parameters

Selecting HIP temperature and pressure is a complex process influenced by several factors. These includes melting point, phase stability, and thermal stability of the materials to ensure effective densification without compromising their structural integrity. TZM has a melting point of 2620°C [27], while NbZr1 melts at 2477°C [2]. As for HIPing, the temperature is usually greater than 0.7 T_m (melting point) [28], which suggests a range of 1700°C–1800°C for these refractory alloy. Additionally, effective porosity removal at the bimetal interface requires deformation of the interfacial grain structure to facilitate microscopic material movement. Moreover, increased diffusivity is necessary to sufficiently close the pores. This also indicates that HIP must be conducted at relatively high temperature to lower the yield strength of both TZM and NbZr1 and

Table 1. Elemental composition (wt.%) of NbZr1 wire and TZM substrate utilised in this study.

Alloying elements (wt%)	Nb	Zr	Ta	O	W	Mo	Hf	C	N	Fe	Al	Ti	Ni
NbZr1wire	Bal.	0.8-1.2	0.5	0.025	0.05	0.05	0.02	0.001	0.01	0.01	0.005	–	0.005
TZM substrate	–	0.1	–	0.04	0.003	Bal.	–	0.01	1 ppm	9 ppm	0.002	0.5	0.005

increase elemental diffusion. For TZM, the yield strength is about 402 MPa at 1200°C and 107 MPa at 1400°C [29]. On the other hand, NbZr1 has a yield strength of around 82 MPa at 1095°C [30]. Therefore, sufficient material deformation can be achieved for TZM-NbZr1 BS above 1400°C with pressures exceeding 110 MPa.

Moreover, microstructural objectives such as grain structure control and phase homogenisation must also be considered during HIP parameter selection. Higher temperatures can induce grain growth in the microstructure which can adversely affect the overall mechanical properties of the structure after HIP. Consequently, it is essential to consider the recrystallisation temperatures of these refractory alloys. Recrystallisation temperature for TZM is around 1400°C [3] and approximately 1200°C for NbZr1 [31]. However, increased pressure can reduce the grain growth effect while reducing the total HIPing cycle. An increase in HIP pressure might also affect phase transformations, alter melting points, and even cause brittle particles to crack, necessitating the careful selection of appropriate HIP pressure. In order to understand the phase transformation behaviour for this bimetal combination under certain temperature and pressure ranges a CALPHAD approach was adopted. Percentage of phases were calculated for a 50:50 mixture of TZM: NbZr1 in the temperature range between 1000°C and 2400°C. The study incorporated three different pressures-50, 100 MPa and 200MPa- with the same temperature range using a FactSage^{TM} software. Interestingly, no significant difference in phase fractions were observed across different pressure conditions.

Figure 2 shows the phase fraction percentages for the TZM-NbZr1 bimetallic structure with a 50:50 composition ratio at a pressure of 200 MPa. The majority of the bimetallic interface is composed of a Body-Centered Cubic (BCC) matrix, along with some carbide phases as indicated in Figure 2(a). Given that the diffusion couple of TZM and NbZr1 contains several carbide-forming elements such as Mo, Ti, Nb, and Zr, the presence of Face-Centered Cubic (FCC) metal carbides (MC) is unavoidable. Previous thermodynamic calculations for TZM have also reported the presence of MC phases [32]. However, as the temperature increases to around 1550°C, these carbide phases begin to dissolve into the BCC matrix. The amount of oxide phases was also calculated and presented separately in Figure 2(b). With the oxygen content considered in the calculation, only ZrO_2 was found as an oxide phase. The calculated quantity of ZrO_2 was higher than that of the carbides. However, unlike carbide phases the phase fraction of ZrO_2 did not show significant variation over the calculated temperature range, as its dissolution requires higher temperatures than those incorporated in the phase calculation [33].

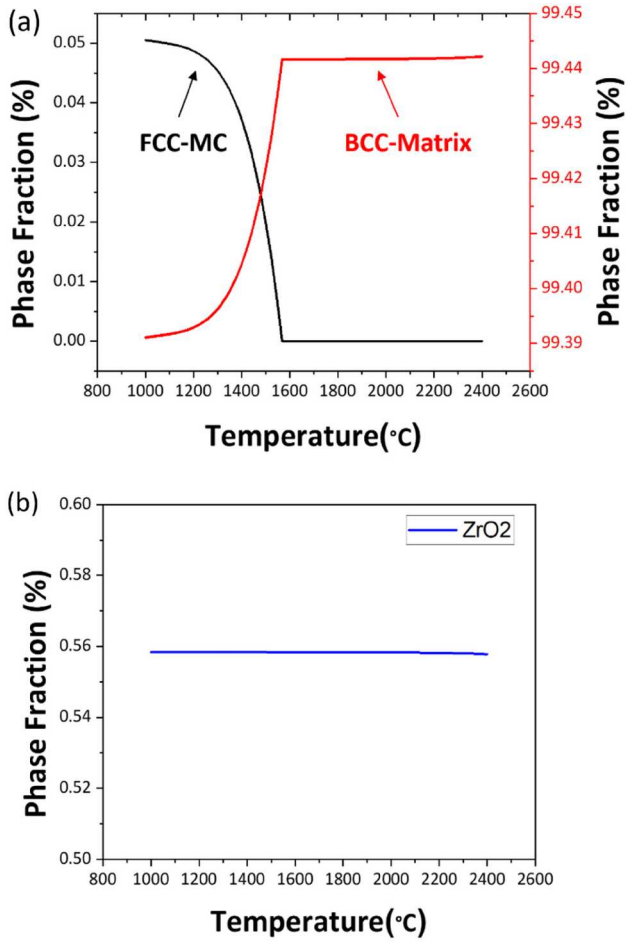

Figure 2. CALPHAD results of 50:50 mixtures (by weight) of TZM: NbZr1 alloy at 200 MPa using FactSage^{TM}:(a) Black line indicates the variation of phase fraction (%) of metal carbide (MC) and the red line indicates the BCC matrix phase, and (b) blue line indicating ZrO_2 phase variation (%) with changing temperature. Mo and Nb-thermodynamic database were employed for phase calculations using the TZM and NbZr1 compositions listed in Table 1.

From the phase calculations, it is clear that there is no major phase transformation at the bimetal interface within the 1000°C–2400°C range, except for the dissolution of carbide phases into the matrix. This dissolution can be advantageous for pore recovery, as reducing carbide particles could enhance material movement during HIPing. Therefore, considering the overall material properties of TZM and NbZr1 and its response to high temperature and pressure, three different conditions were selected for investigation: HIP-1 (1200°C, 200 MPa, 3hrs.), HIP-2 (1500°C, 200 MPa, 3 hrs.), and HIP-3 (HIP at 1800°C, 200 MPa, 3 hrs. followed by heat treatment at 1000°C, 100 MPa, 2 hrs.). These HIP parameters are schematically represented in Figure 3.

The final heat treatment temperature in HIP-3 condition was carefully chosen to avoid causing any

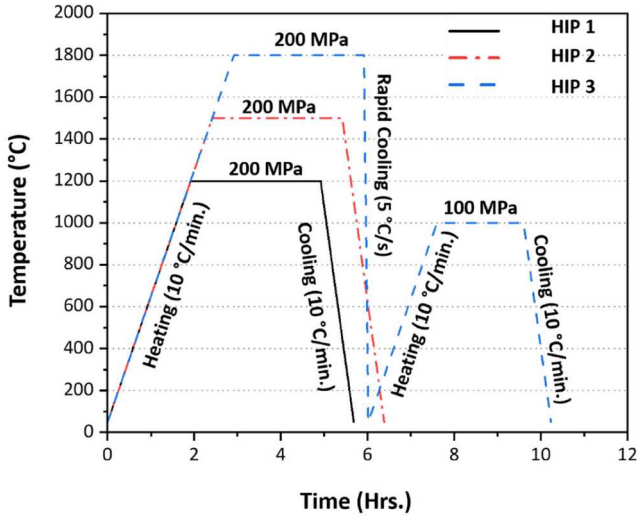

Figure 3. A schematic diagram showing the temperature and pressure cycles of HIP-1, HIP-2, and HIP-3 condition.

recrystallisation in the microstructure. The primary goal was to assess whether re-precipitation would occur, similar to an aging treatment, following rapid cooling from 1800°C. Prior to the HIP treatments, all samples underwent stress relief in a vacuum furnace at 1100°C for 50 min. A pressure of 200 MPa was used during the HIP-1 and HIP-2 processes, which were carried out in a QIH 15L molybdenum furnace with a Uniform Rapid Cooling (URC®) system utilising 99.995% argon at Quintus Technologies LLC in Ohio, USA. The URC system provides precise control over pressurisation and cooling, essential for achieving accurate treatment results. In the HIP-3 (HIP + HT) treatment, the heat treatment cycle was conducted under a reduced pressure of 100 MPa in a QIH 15L graphite furnace with the URC system at the same facility.

2.3. Pore assessment

For macro-level porosity analysis, cross-sectional samples were examined. The cross-sectional area of the deposits underwent mirror-finish polishing, allowing for exclusive recognition of pores during porosity assessment. From each cross-section, 20 Optical Microscope (OM) images were collected across different areas and then converted to binary images with a constant threshold using ImageJ software [3]. The analysis involved calculating the pore diameter and pore area fraction.

2.4. Material characterisation

Characterisation of the as-built and HIP-treated samples involved transverse sectioning using wire electrical discharge machining (EDM). Subsequently, the sectioned samples were hot mounted in Bakelite thermosetting powder. Metallographic preparation followed, employing grinding wheels with sandpaper (SiC abrasives) of varying grits (240, 400, 600, 800, and 1200) and diamond paste solutions with particle sizes of 3 and 1 µm. Etching procedures were specifically tailored for the TZM and NbZr1 sides, utilising Murakami's reagent [10 g KOH, 10 g $K_3Fe(CN)_6$, and 100 mL H_2O] and solution of 10 mL HF + 10 mL HNO_3 + 30 mL lactic acid, respectively. For optical microscopy (OM), a Nikon SMZ 1500 microscope was used for the low-magnification images (up to 50× magnification), and a Nikon Epiphot inverted microscope was employed for the high-magnification images (up to 100× magnification). A Hitachi SU 7000 scanning electron microscope (SEM) equipped with an Octane Elect Super energy-dispersive X-ray spectroscope (EDS) was used for the microstructure and chemical composition analysis. The samples were also characterised using X-ray diffraction (XRD) analysis. The XRD measurements were performed using a Rigaku Ultima IV equipped with an X-ray tube (3-kW sealed) and a detector (D/teX Ultra silicon strip). The X-rays were produced at 30 mA and 40 kV with Cu Kα radiation having a wavelength of 0.15 nm.

3. Results and discussion

3.1. HIP effect on pore

Figure 4(a–d) shows the cross-sections for as-built, HIP-1, HIP-2, and HIP-3 samples. Notably, majority of the pores were found at the bimetallic interface for as-built samples, which is consistent with the findings from a prior study of TZM/NbZr1 [13]. The samples contained numerous SSPs, IPPS, and large pores as shown in

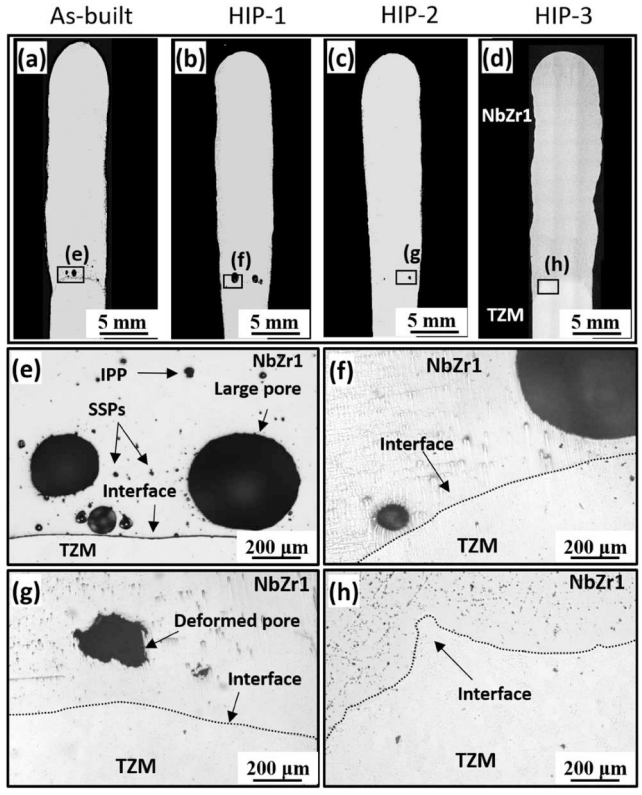

Figure 4. OM images from the unetched cross-section of (a) as-built, (b) HIP-1, (c) HIP-2, and (d) HIP-3 sample showing the pores at the bimetal interface; (e) magnified view of the interface (black rectangle) from image (a), (f) magnified view from image (b), (g) magnified view from image (c), and (h) magnified view from image (d).

Figure 4(e). SSPs, which have a diameter of less than 190 µm, were uniformly distributed throughout the interface while large pores having a diameter greater than 190 µm had non-uniform distribution. On the other hand, a few IPPs were present at the interfacial region between TZM substrate and NbZr1 deposit, which were formed due to the contact of two pores with different diameters [3].

Following HIP-1, the porosity level was similar to the as-built condition, but a significant pore reduction was evident after HIP-2. Deformation and transformation of spherical pore surfaces into irregular shapes were also noticeable as shown in Figure 4(g). Although SSPs had decreased extensively in HIP-2 samples, large pores did not recover completely. However, after HIP-3, complete

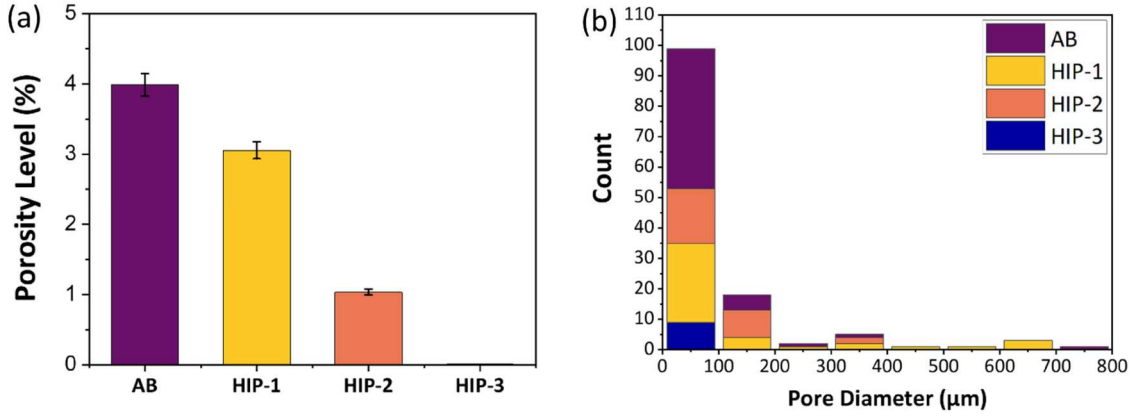

Figure 5. (a) Average Pore area fraction (in %) of all conditions indicating porosity level in the cross section of TZM/NbZr1 bimetal interface (calculated using ImageJ software) and (b) Histogram of pore size (diameter) distribution at the interface before and after HIP treatments.

removal of porosities was seen from the cross-sectional image in Figure 4(h). In addition, deformation in the bimetallic interface suggests increased interface movement for higher HIP temperature.

Figure 5(a) shows the quantitative comparison of the measured porosity levels in as-built, HIP-1, HIP-2, and HIP-3 samples. The as-built samples had a total pore area fraction ranging from 3.96% to 4.05%. After HIP-1 and HIP-2 treatments, the total area fraction of pores were measured as 3.05% and 1.01%, respectively. For HIP-3 condition, the porosity level was found to be approximately 0.01%. This shows that the overall pore area fraction was reduced by 25%, 75%, and 99.75% as a result of the HIP-1, HIP-2, and HIP-3 treatments, respectively. In Figure 5(b), the pore size distribution for all the conditions is summarised. In the as-built condition, the maximum pore diameter was measured 700–720 µm, although majority of them were less than 100 µm. For the HIP-1 condition, the pore size distribution closely resembles the as-built condition, with a maximum pore size of 650 µm. In contrast, the HIP-2 case displays a maximum pore size of approximately 390 µm. This indicates that pore size had decreased significantly during HIP-2 even though complete healing of large pores did not occur. The HIP-3 case exhibited negligible porosity, as evidenced by the cross-sectional image in Figure 4(d, h).

3.2. HIP effect on microstructure

Figure 6 shows the microstructure of TZM/NbZr1 BS interface for the as-built condition. The microstructural characteristics are consistent with the observations in previous study [13]. The grain structures, illustrated in Figure 6(b), display epitaxial grains coherent with the TZM substrate, typical of the WAAM process [34]. Equiaxed grains are also visible as shown in Figure 6 (c), although they are less prevalent compared to the columnar grains. Pores of varying sizes extending throughout the entire thickness of the thin wall were also identified. These pores on the NbZr1 side are primarily due to the presence of Mo, as the main source of pores is attributed to the formation of MoO_3. EDS mapping in Figure 6(d1–d4) also reveals diffusion of Mo into the Nb side, with negligible Nb diffusion in the TZM. Apart from the Mo and Nb, Zr had a homogeneous distribution throughout the interface as both of these alloys contain Zr as major alloying element. Figure 6(e) depicts the microstructure near a pore, while Figure 6(f) shows the microstructure away from pore within the mixing zone. Remarkably, no substantial difference was observed in the microstructure between areas surrounding and away from the pores in the as-built condition. However, numerous particles with irregular sizes and shapes were seen at the grain boundaries. Figure 6(g) highlights these particles at the mixing zone, identified as ZrO_2, which formed due to Zr's high affinity for oxygen [35]. The NbZr1 wire contains about 0.025 wt.% of oxygen, and Zr can absorb oxygen during the deposition process, resulting in ZrO_2 formation. The presence of ZrO_2 particles in WAAM-deposited NbZr1 was also reported in a previous study [2]. Additionally, minor carbide presence near the oxide particles was identified, as highlighted with an EDS line scan in Figure 1(h). As the TZM alloy is known for containing numerous carbide formers, presence of these carbide precipitates is inevitable [3].

Compared to the as-built sample, no significant changes in the grain structure were observed after HIP-1. However, partial deformation of spherical pore surfaces into irregular shapes was identified. This transformation is likely a result of limited material deformation in this condition. After HIP-2, a few areas with recovered pores were identified at the interface, although complete removal of certain large pores were not evident. A radial change in material morphology adjacent to the deformed pores and near the pore closure region was observed, as shown in Figure 7(b-2). This can be attributed to the direction of material flow and stress transmission during HIP [36]. A crucial feature of the microstructure after HIP-1 is the presence of microcracks and voids at the interface closer to the NbZr1 side. In Figure 7(a-2), the presence of cracks across the epitaxial grain boundaries is visible. The formation of such internal defects can originate from the pre-existing crack at the edge of the thin wall. Figure 7(a-3) shows the WAAM-induced crack at the edge of the as-built sample, and the connectivity of the microcracks travelling mostly through the weak spots of grain boundaries at the interface. Non-equilibrium thermal cycles experienced by the structure during deposition can result in residual stresses, which can lead to crack formation immediately after cooling from the molten state [37]. Besides, major difference in the CTE between the TZM and the NbZr1 alloy can contribute to this phenomenon. These microcrack near the interface are more prominent for HIP-1 compared to HIP-2 mostly due to the deformation force imposed on the structure at HIP-1 when it exhibited limited plasticity. Furthermore, work hardening during the initial stage of the HIP cycle can also stiffen the BS, increasing material flow stress, which has a detrimental effect on the crack propagation resistance of the interface [38]. On the other hand, micro-voids were observed at the interface after HIP-2, as shown in Figure 7(b-3). These voids are likely formed to

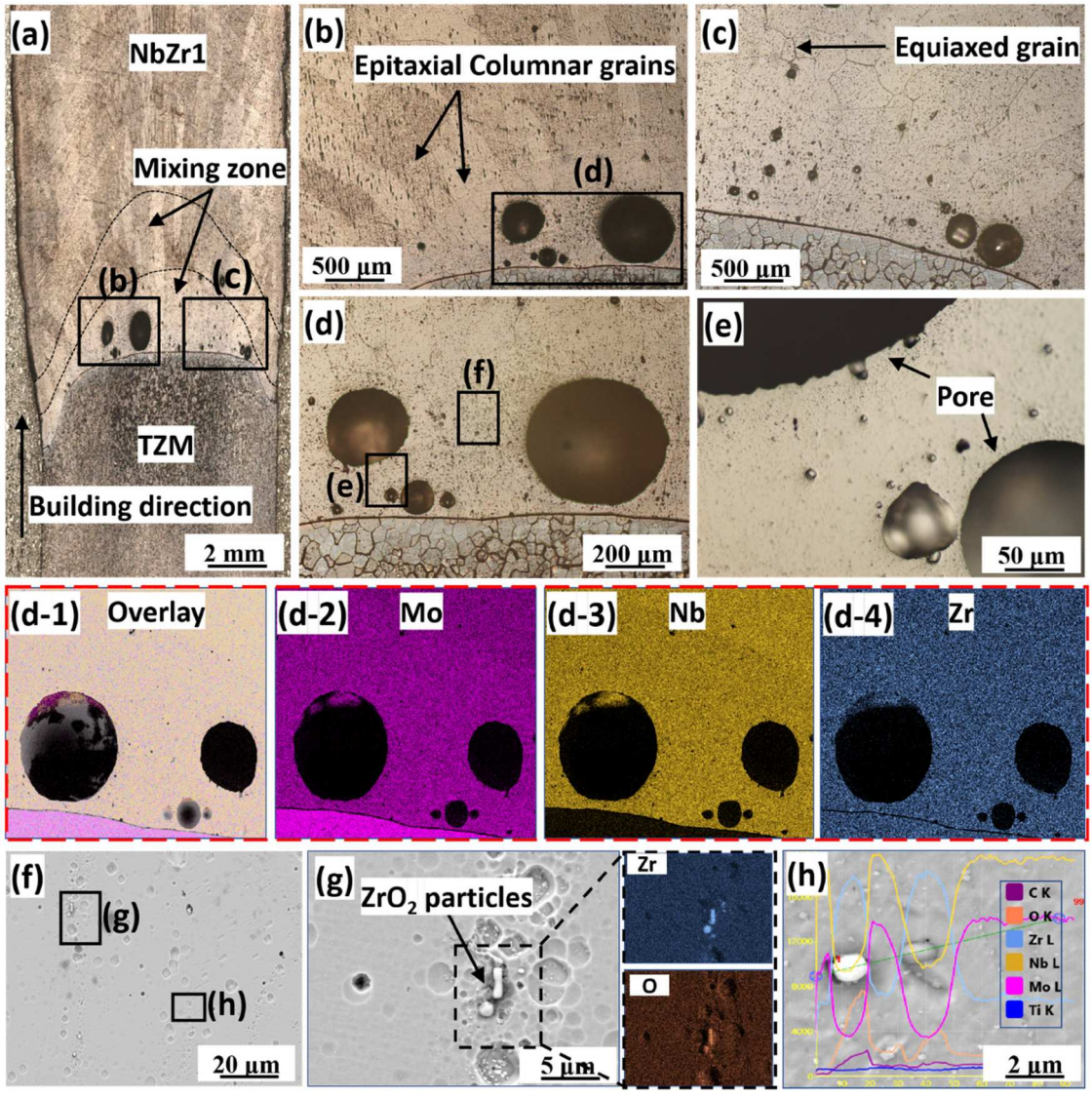

Figure 6. (a) Stitched image from the cross section of TZM/NbZr1 interface after etching, (b) epitaxial columnar grains, (c) equiaxed grains, (d-e) pore structures, (d1-d4) EDS area mapping from black rectangle in image (d) showing the presence of different element at the interface, (f) grain boundary area from image (d), (g) magnified image of ZrO_2 particles from (f), (h) magnified view of oxide and carbide particles with EDS line scan from image (f).

facilitate additional plasticity owing to the accumulation of stresses near the pore. Detail discussion about these micro-voids is presented in Section 3.3.

The microstructure of the TZM/NbZr1 interface after HIP-3 is shown in Figure 7((c-l)–(c-3)). Following HIP-3, large pores were not observed, with a significant presence of recrystallised grains identified within the pore-recovered regions. The grain boundary epitaxy was maintained correlating to the grains of the TZM substrate. Coarse grains of the as-built sample were replaced by finer recrystallised grains near the pore recovered area, while the microstructure away from the pores remains analogous to the as-built condition, comprising of epitaxial columnar grains. In addition, bulging of the grains are also visible from Figure 7(c-1) which can be correlated to the incidence of recrystallisation. Compared to HIP-1 and HIP-2 condition, HIP-3 condition is free of cracks or voids. Besides, the extension of the interface line movement is comparatively greater indicating increased amount of plastic deformation. The absence of cracks or micro voids in this condition can thus be attributed to reduced flow stress during HIP. Pore-recovered areas were easily identified by the presence of smaller equiaxed grains, likely formed during fast cooling (5°C/s) from 1800°C. Interestingly, these finer grains are situated closer to the area where the material experienced the most deformation, suggesting a correlation between the pore recovery mechanism and an increased amount of plastic deformation.

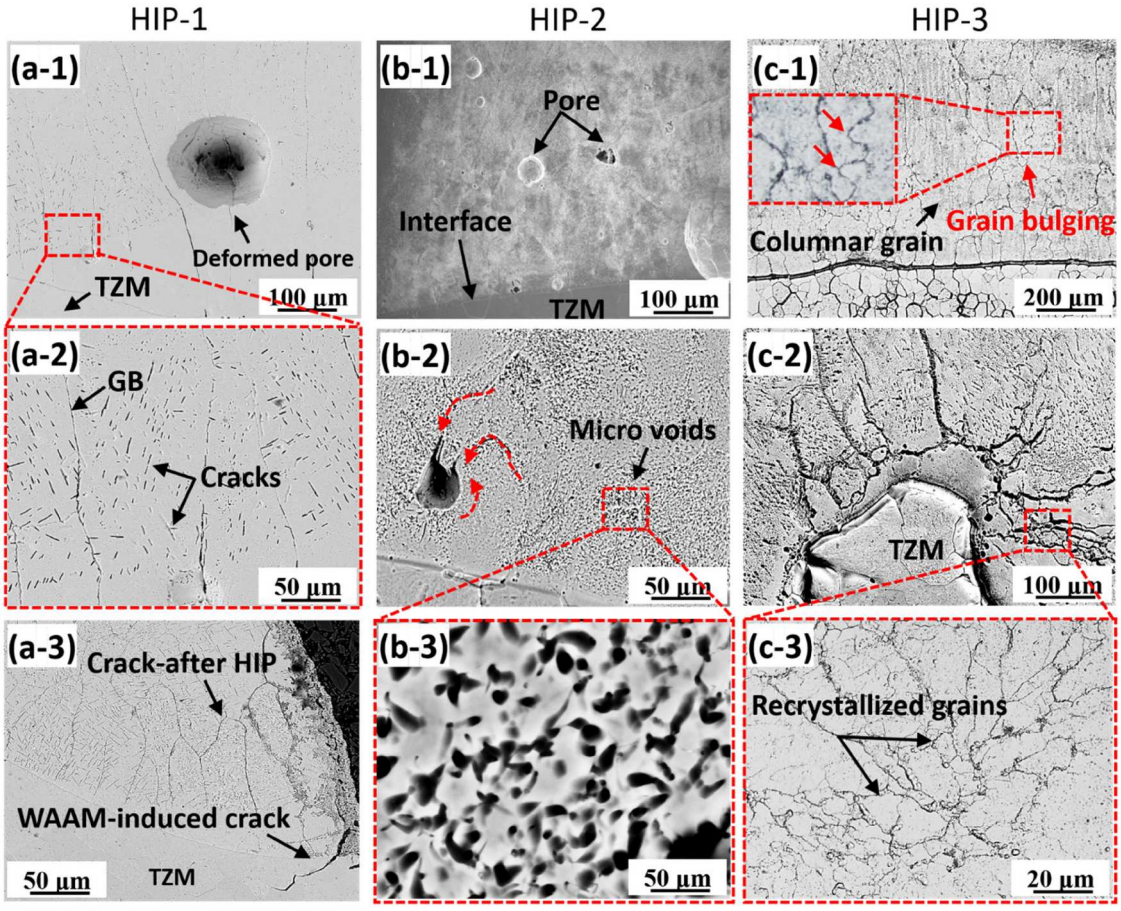

Figure 7. SEM images of the bimetal interface; ((a-1) -(a-3)) after HIP-1, ((b-1) -(b-3)) after HIP-2, and ((c-1) -(c-3)) after HIP-3.

Nb and Mo have good solubility in each other above 2400°C and can form substitutional solid solutions due to the smaller difference in lattice parameters or atomic radii [39]. However, at room temperature, there is limited solubility of Mo and Nb, resulting in the presence of pure Mo and Nb phases in the as-built condition. In addition, no intermetallic compounds between Mo and Nb were observed at the TZM/NbZr1 interface after HIP treatments. The existence of pure Mo and Nb phases in the as-built condition at the TZM/NbZr1 interface was also mentioned in a previous study [13]. Yet, the possibility of a phase transformation at the interface for different HIP temperatures cannot be avoided due to the presence of minor alloying elements i.e. Ti, Zr, and C. The ternary diagram of Mo-Nb-Zr system suggests the presence of BCC (β) and Laves phases [40], whereas the Mo-Zr-Ti ternary system indicates phases consisting of a single-phase region (β) and two two-phase regions (β1 + Laves and β2 + Laves) [41].

Therefore, in order to observe the effect of HIP on phase transformation and to compare with the phase calculation results presented in Figure 2, X-ray diffraction (XRD) analysis was conducted at the interface of TZM/NbZr1 bimetal structure for all the experimental conditions. XRD spectra were collected in the scan range of 2θ = (20°- 90°) with a step width of 0.02°, as shown in Figure 8. Primary peaks were identified at 2θ values of 38.05°, 40.14°, 55.22°, 58.25°, 68.96°, and 73.25° in the as-built condition. Pure Mo and Nb phases were confirmed based on the peak positions, as illustrated in Figure 8(a). The presence of ZrO_2 is also indicated by XRD peaks for all experimental conditions. In the as-built condition, Nb peaks were similar to the β-Ti peak due to their close X-ray intensity, suggesting the possibility of forming solid solution of (βTi,Nb) [42]. However, considering the significant difference in composition between Nb and Ti at the interface, these peaks were recognised as Nb. Besides, the (Nb,Ti) solid solution was not identified as a distinct phase from the microstructure. The detection of pure Mo and Nb phases is also consistent with findings from a previous study [6]. In addition to the pure phases, minor peaks were observed for all conditions. XRD analysis indicated the potential presence of small amounts of Mo_2C, TiC, ZrC, and TiO_2, although their intensities were not high enough for a strong identification in the spectra.

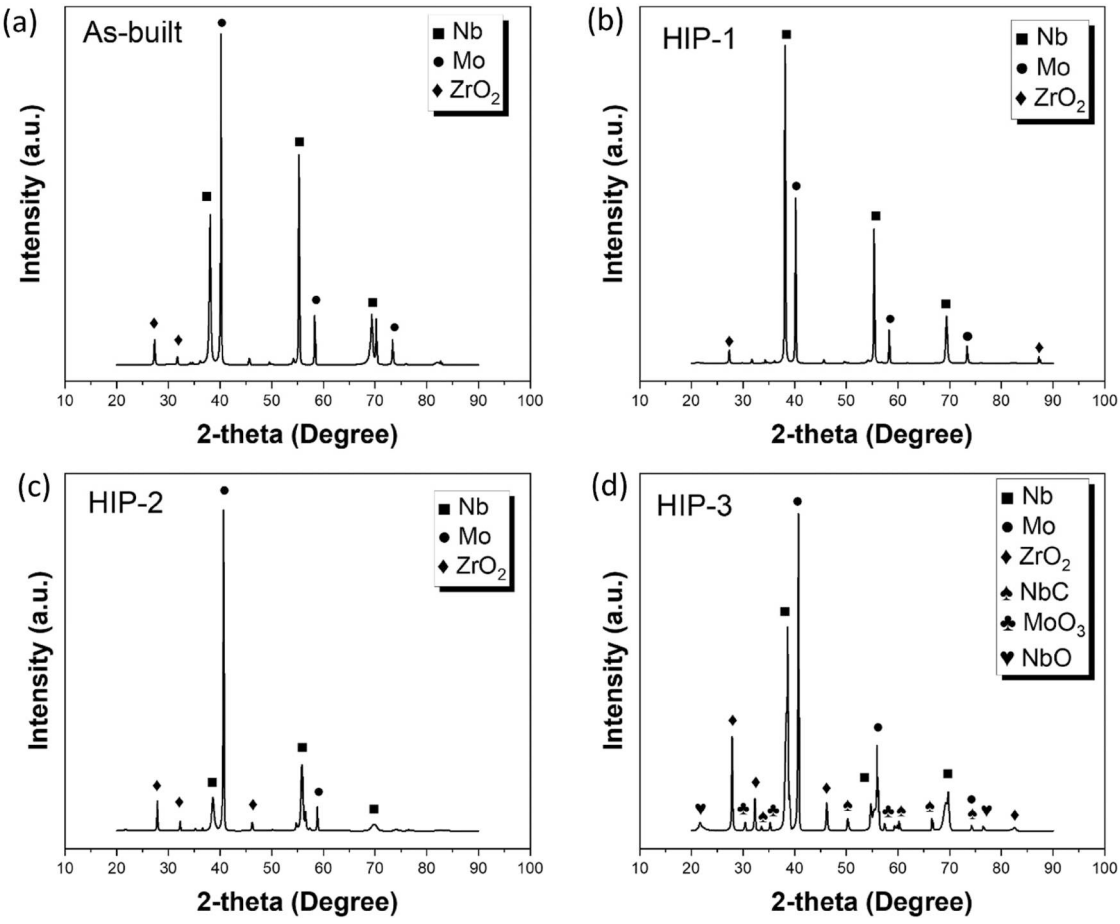

Figure 8. XRD spectra from the bulk structure including bimetal interface for (a) as-built, (b) HIP-1, (c) HIP-2, and (d) HIP-3 condition.

Compared to CALPHAD predictions carbide phases were less evident in the X-ray diffraction (XRD) analysis likely due to the low carbon content in the TZM and NbZr1 composition. While some carbon was observed in the EDS spectra near the interface (in the as-built condition), majority of these phases were located on the TZM side. Figure 8(d) illustrates the XRD peaks for the sample after HIP-3 treatment, revealing an increased number of small peaks associated with oxides in the scattering angle range of 20°-70°.

A small amount of NbC was detected in the HIP-3 sample, likely due to the dissolution and re-precipitation of carbides. Although NbC typically forms at higher temperature (above 1800°C), as indicated by the Nb-C phase diagram, [43], previous experiments have shown that NbC can form as low as 1300°C in Nb alloys containing high amount of carbon, such as Nb-1Zr-0.1C [44]. In the present study, the amount of carbon in the parent alloy composition is very low, 0.01% and 0.001% for TZM and NbZr1 respectively. Therefore, the presence of NbC after HIPing can be attributed to the increased amount of carbon diffusion into the Nb-side with increased HIP temperature. However, NbC was not detected in the XRD spectra of HIP-1 or HIP-2 sample, indicating that faster cooling and subsequent heat treatment in HIP-3 were crucial for increasing carbide precipitation. Rapid cooling from 1800°C resulted in supersaturated Nb-C solid solutions that trapped carbon in the niobium matrix. The subsequent heat treatment at 1000°C then promoted increased re-precipitation of the carbide phase. Supersaturation and re-precipitation of NbC have also been observed during heat treatment in previous studies [45, 46]. Niobium carbides are crucial in enhancing the high-temperature strength of niobium-based alloys by improving thermal stability, creep resistance, and resistance to liquid alkali metal corrosion. Therefore, the formation of NbC would be beneficial for the TZM/NbZr1 BS which can improve its high-temperature performance.

In addition to the carbide phase, certain oxide phases such as ZrO_2, NbO and MoO_3 were also identified in the spectra. The increased presence of ZrO_2 compared to HIP-1 and HIP-2 condition was likely due to the accumulation of particles during the heat treatment cycle following the rapid cooling from 1800°C. ZrO_2 usually increases hardness of the NbZr1 system [2], however if

Zr-O coherent zone is created it could strengthen the Nb-Zr1 while reducing its ductility. If sufficient oxidation occurs, causing all the Zr in Nb-Zr1 to fully react and form ZrO_2, subsequent oxidation could lead to the dissolution of interstitial oxygen into the Nb matrix, which may eventually result in the formation of NbO phases. [47]. As oxygen usually diffuses as an interstitial solute, formation of NbO would require increased driving force which can facilitate sufficient diffusion. This suggests that detectable levels of NbO are more likely to be present in the HIP-3 condition, where increased oxygen diffusion into the niobium matrix is facilitated. However, given the lower formation temperature of NbO (around 600-700°C), formation of NbO is inevitable in both HIP-1 and HIP-2 cases [48]. Therefore, the absence of this phase under lower HIP conditions can be attributed to the lower amount of NbO present, which is below the detectable limit of XRD. While NbO behaves like a metal and exhibits good superconducting properties, its impact on the mechanical properties of the bulk structure remains uncertain and warrants further study [49]. Presence of MoO_3 can be attributed to the lower heat treatment temperature in HIP-3 whereas the HIP-1 and HIP-2 condition experienced higher temperature than the boiling point of MoO_3. MoO_3 can improve the toughness of the material by increasing the Young's modulus. However, the positive impact largely depends on the coherency of this phase within the matrix. Besides, as it has lower boiling temperature, it can reduce thermal stability of the bimetal interface [50]. The XRD results reveal that most of the phases observed in the microstructure were accurately predicted by the phase calculations. However, the formation of secondary phases after the heat treatment of HIP-3 was not anticipated in the equilibrium cooling results, as the subsequent aging effect was not considered in the calculations.

Among the various secondary phases identified in the XRD analysis, ZrO_2 is the most prominent in the microstructure. In order to qualitatively assess the distribution and size of ZrO_2 under various HIP conditions, EDS mapping was performed. Figure 9 represents the ZrL spectra for all the different experimental conditions. It is evident that the distribution is random for as-built, HIP-1, and HIP-2 condition. However, for HIP-3 condition, oxide particles were more homogeneously spread within the microstructure, indicating increased movement of these particles during the HIP cycle, consistent with the XRD results.

In order to further analyse the compositional configuration at the interface, EDS line scans were conducted along the building direction for different HIP

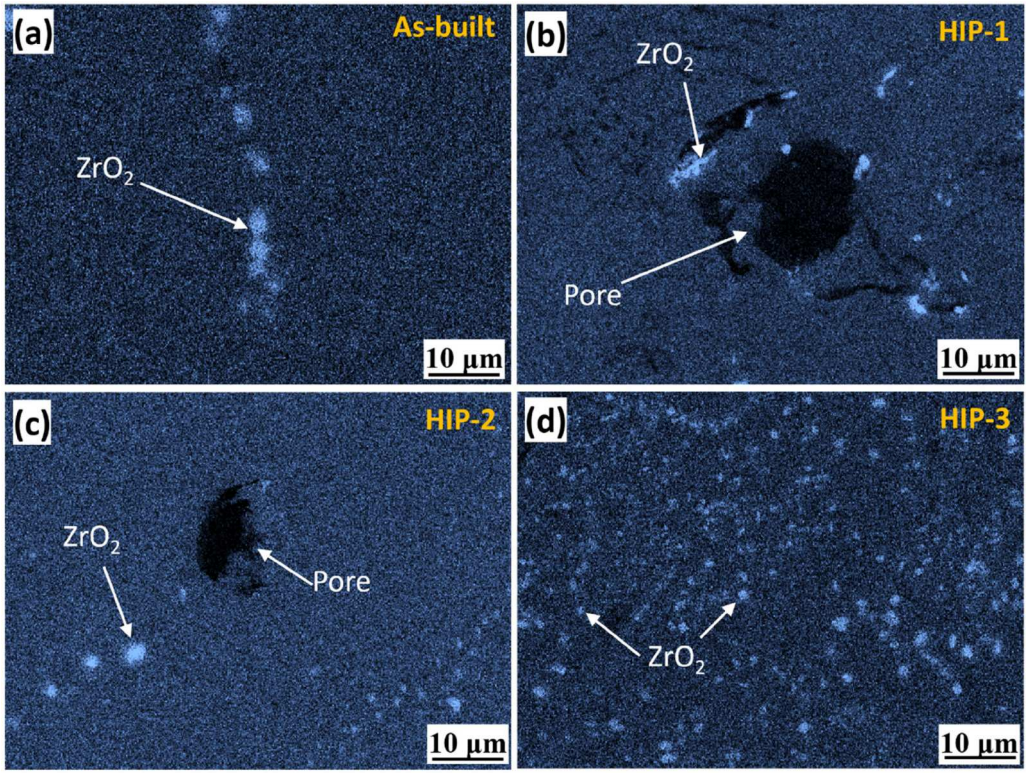

Figure 9. Distribution of ZrO_2 at the interface of (a) as-built, (b) HIP-1 (b), (c) HIP-2, and (d) HIP-3 condition indicated by ZrL spectra from EDS area mapping.

conditions. Figure 10 presents a comparison of elemental line scans starting from the TZM substrate and ending in the NbZr1 side. The total distance of the line scan was 13 mm for as-built condition and 10 mm for HIP conditions, encompassing the TZM-NbZr1 interface. A significant difference in elemental concentration after HIP treatment is evident. The change in Mo composition at the interface is abrupt for all conditions, compensating for the sudden increase in Nb counts from the beginning of the interface. This can be attributed to the reduced interdiffusion coefficient of Nb in Mo-rich substrate [51].

However, the compositional difference between Mo and Nb at the interface was reduced after HIP, as evident from the reduced gap between Mo and Nb counts in Figure 10(b) and (c). This observation also suggests an increased diffusion of Mo into the Nb matrix after HIP which is mostly due to the increase in interdiffusion coefficient of Mo into the BCC Nb matrix with increasing temperature [51]. The total diffusion length of Mo increased with the rising HIP temperature from HIP-1 to HIP-2 condition. However, for the HIP-3 condition as seen in Figure 10(d), the diffusion depth of the Mo is not as high as HIP-1 and HIP-2 which is mostly due to the reprecipitation of the carbides close to the interface during the subsequent HT process. The irregularities in the continuous compositional data for both TZM and NbZr1 indicate the presence of oxide and carbide particles along the scanned line, accompanied by an increase in the intensity of Ti and Zr.

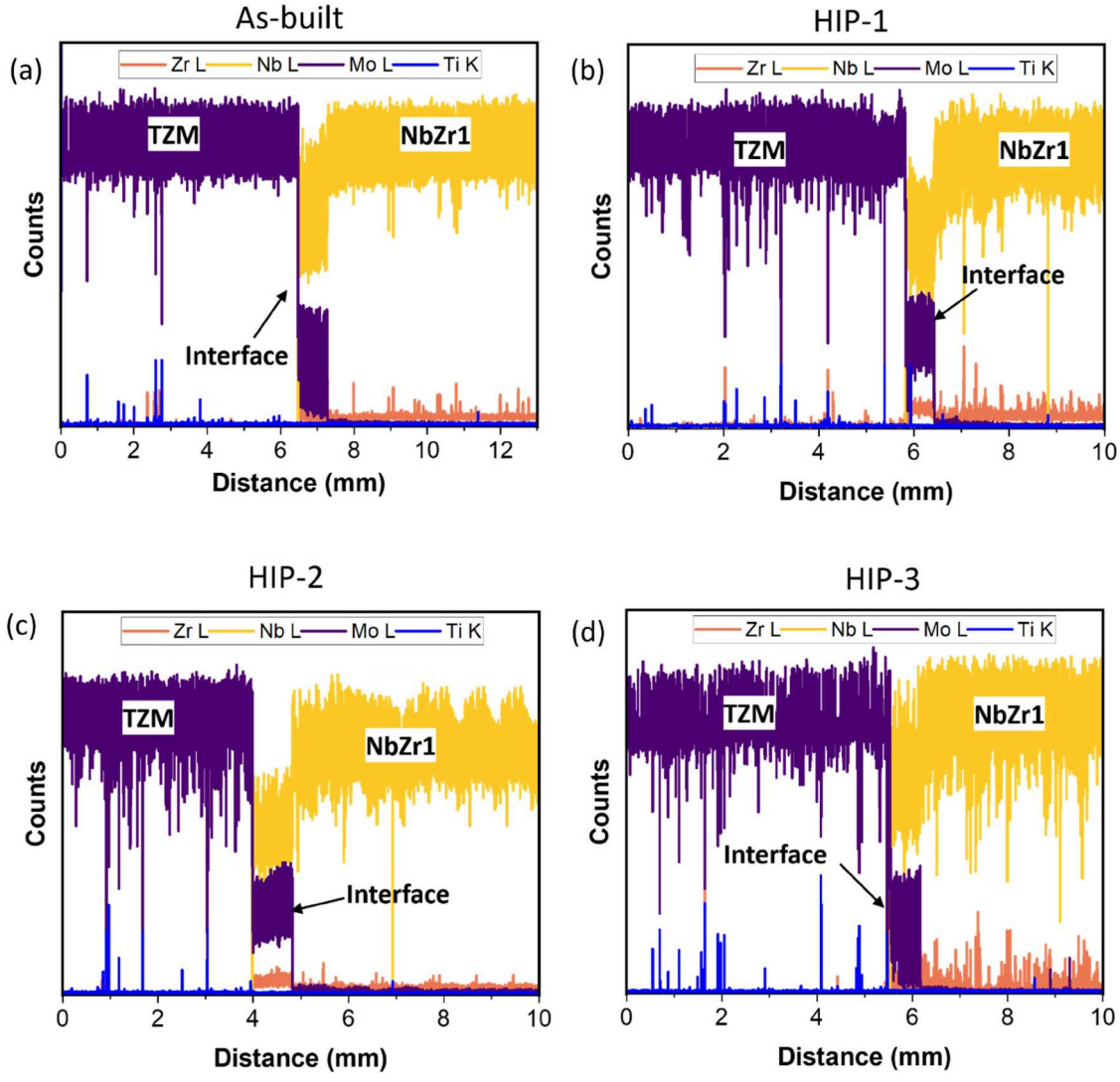

Figure 10. EDS line scan across the interface showing variation in the elemental composition by counts for (a) as-built, (b) HIP-1, (c) HIP-2 and (d) HIP-3 samples.

3.3 . Pore recovery mechanism

3.3.1. HIP treatment at 1500°C (HIP-2)

Typically, the size of gas pores is reduced due to surface-energy driving forces, which are counteracted by the gases inside the pores. During HIP, the applied external isostatic pressure amplifies these forces, causing the gases to dissolve into the surrounding material [28]. The net force exerted on the pore surface is inversely proportional to the pore radius [52]. Consequently, in small spherical pores, the force acting on per unit area is comparatively greater than that experienced by larger pores. This results in a rapid reduction of SSPs during the initial stages of pressure application. In contrast, the force acting per unit area on larger pores is smaller, leading to less material flow within these pores. As seen in Figure 3(c), it is apparent that most of the SSPs disappeared after HIP-2, while some deformed large pores were still present. In many cases of casting defects, densification begins with the removal of large pores by macroscopic plastic flow prior to the isothermal stage of the HIP cycle [28]. However, the presence of large pores after HIP treatment of this BS indicates that the pore closure mechanism could differ from that observed in casting.

Figure 11(a) shows the SEM images of the interface after HIP-2, revealing several partially healed pores. Application of high pressure above the recrystallisation temperature of both TZM and NbZr1 induces plastic deformation in the microstructure, which is more pronounced near the pore surfaces. The hydrostatic pressure generated during HIP compresses the material around the gas pores, thereby reducing the pore volume, as illustrated in Figure 11(b–d). Notably, pores near the grain boundary experience significant deformation compared to those farther away. Movement of the boundaries can also be traced by following ZrO_2 particles, which align with the direction of material flow. Figure 11(b) shows the location and arrangement of these particles near the pore area. Many of these particles are present along the epitaxial grain boundary (Figure 11(c)), indicating that the epitaxial grain boundary also underwent significant migration in response to the applied temperature and pressure. Grain boundary migration has also been identified by previous researchers as a common phenomenon during HIP of alloys such as 316L stainless steel [53].

In addition to grain boundary movement, the presence of micro-voids near the pore-recovered area is apparent, as depicted in Figure 11(e). Although the formation of micro-voids during HIP is unexpected, the images suggest a correlation with material movement, as these voids primarily appear near the deformed pores. This observation can indicate the prevalence of diffusion during HIP, which can facilitate pore healing in conjunction with plastic deformation. Formation of micro-voids after HIP is rare in existing literature. Chen et al. observed micro-voids after HIP at 1800°C in L-PBF-produced pure tungsten [26]. They attributed the presence of micro-voids to the diffusion bonding and healing of the cracks existing in the as-deposited microstructure. The formation of micro-voids in the present study can be attributed to several factors inherent to the HIP process, particularly the complex interplay between diffusion, plastic deformation, and stress gradients.

During HIP, the high temperatures and pressures induce significant material movement, which is critical for closing larger pores. However, as the material flows to heal these pores, local stress gradients can develop around the pore surface, particularly during the initial stages of HIP when the material is still accommodating the applied pressure. These stress gradients are likely to form at interfaces, such as those between the Nb and Mo matrices, due to their differing responses to the applied thermal and mechanical loads. The differences in thermal expansion coefficients, yield strengths, and creep behaviours between the two materials can result in uneven stress distribution, especially near the pore surfaces. Stress accumulation along the pore surface during HIP is frequently reported in literature [54] which can promote the development of complex dislocation structures. The ongoing accumulation of stress during the isothermal stage of HIP can induce these dislocation structures, particularly around the pore areas. These dislocations can act as pathways for the slipping of material, which in turn facilitates the diffusion of vacancies. As the vacancies migrate, they can coalesce into micro-voids, particularly in regions of high stress concentration where localised decohesion may occur [55]. This decohesion is likely a consequence of the material's inability to sustain the accumulated stress, leading to the formation of voids as the material attempts to relieve the stress. Moreover, the interaction between plastic deformation and diffusion is critical in this context. As the material deforms plastically, the mobility of dislocations increases, which can further enhance the vacancy diffusion process. The localised slipping of material near these micro-voids, as shown in Figure 11(f), is indicative of micro-deformation at these high-stress locations.

The slipping not only facilitates material flow but also redistributes the material, breaking down the overall pore area into smaller units, thereby contributing to pore recovery. The presence of large voids, as shown in Figure 11(h) also indicates the prevalence of

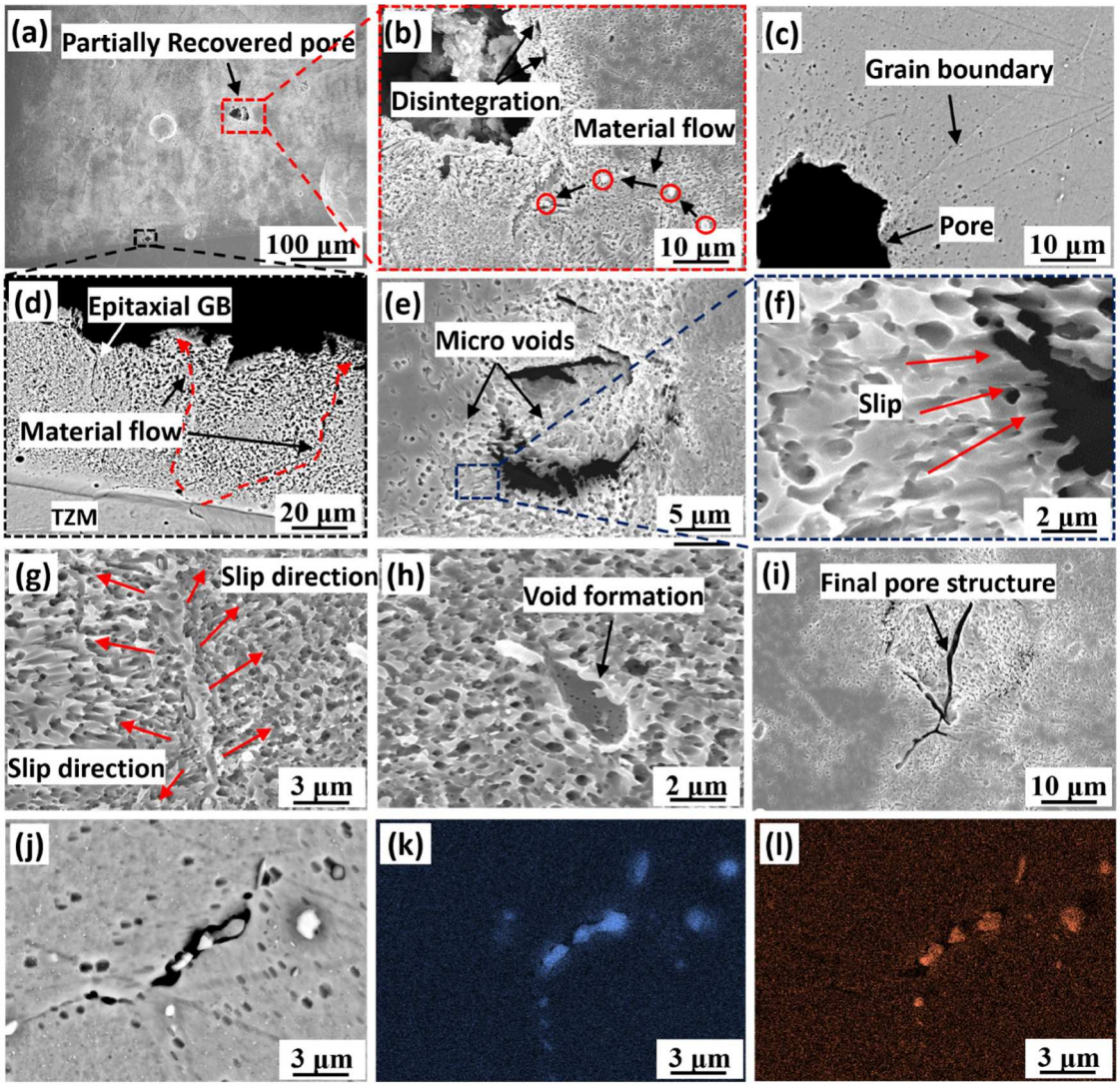

Figure 11. SEM images at the interface after HIP-2 showing (a) partially recovered pores, (b) magnified view of a deformed pore from image (a) with particles following material flow direction around the pore area, (c) deformed pore and correlating grain boundary, (d) material flow and epitaxial grain boundary movement close to the substrate, (e) presence of micro-voids near the recovered pore, (f) slipping near the micro voids (g) difference in slipping direction, (h) void formation due to vacancy coalescence, (i) final pore structure, (j) particle accumulation near recovered area, and (k), (l) represents EDS elemental maps for Zr L, and O K spectra corresponding to image (j) respectively.

vacancy diffusion during HIP-2. Additionally, the movement of oxide particles observed in Figure 11(b) can be correlated to the material's slipping behaviour. As the material flows under the influence of stress and temperature, the oxide particles, which are typically harder and more brittle, tend to follow the slipping direction of the matrix. These particles can accumulate at the pore-recovered area, potentially influencing the local microstructure and the stability of the healed pores. Figure 11(j) highlights the accumulation of ZrO_2 particles in the pore-recovered zone. EDS area mapping of the pore-recovered location from Figure 11(j) is presented in Figure 11(k, l). The presence of ZrO_2 is evident from the Zr L and O K spectra.

The overall pore closure mechanism under HIP-2 treatment is schematically presented in Figure 12. At the beginning of the HIP application, the pores on NbZr1 side adjacent to the interface are mostly spherical (Figure 12(a-1)). As the HIP pressure and temperature increase, plastic deformation of the material initiates at areas surrounding the pore, causing the spherical pore surface to adopt an irregular shape (Figure 12(a-2)). The hydrostatic pressure compresses the material surrounding the pores, reducing their volume, with significant deformation observed near the grain boundaries. Throughout the holding period, during which isostatic pressure is applied at elevated temperatures, material flow persisted, leading to partial pore closure (Figure

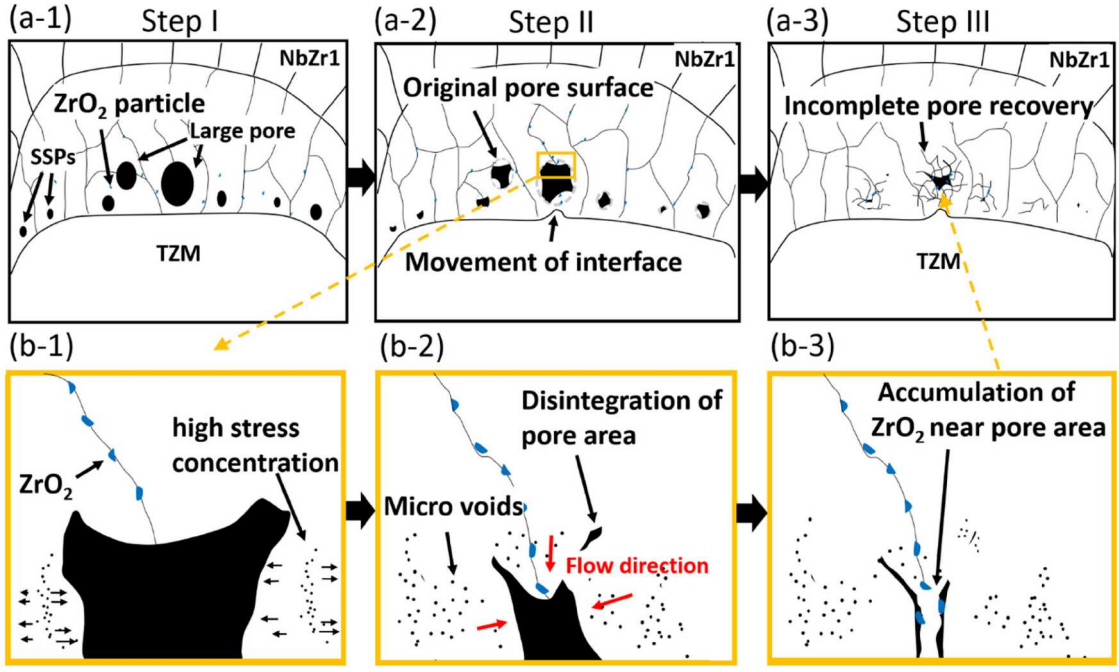

Figure 12. ((a-1)–(a-3)) Schematic diagram of overall pore recovery process during the isothermal stage of HIP at 1500°C; ((b-1)–(b-3)) magnified view from yellow rectangle shown in (a-2) illustrating underlying recovery mechanism.

12(a-3)). During this process, local stress gradients form around the pore surfaces, especially at the interfaces between different materials like Nb and Mo, due to their varying thermal and mechanical properties. These stress gradients can lead to the formation of dislocation structures that facilitate material slipping and vacancy diffusion, resulting in micro-void formation in areas of high stress concentration. Moreover, ZrO_2 particles accumulated along the grain boundary following the material flow. Figure 12(b-1) provides a magnified view from a location of high stress concentration surrounding the pore region from Figure 12(a-2), which is indicated by a yellow rectangle. Figure 12(b-2 and b-3) displays the increased material flow and the formation of micro-voids along with the accumulation of ZrO_2 around the pore during the pore recovery process.

3.3.2. Integrated HIP treatment at 1800°C + heat treatment (HIP-3)

For HIP-3 condition, the pore recovery process is primarily attributed to the increased plastic deformation occurred in the HIP cycle. This is because, during the subsequent heat treatment (HT) cycle, the material experiences minimal plastic deformation due to its higher strength following rapid cooling from 1800°C. Additionally, the heat treatment temperature is not sufficient to induce significant deformation at the interface. In the post-HIP microstructure, the transition from columnar to equiaxed grains near the pore is evident, as observed previously in Figure 4, indicating that recrystallisation has occurred in these regions. Recrystallisation during pore closure was also reported by previous studies of HIP [56, 36].

The SEM images in Figure 13(a–c) provide a detailed view of this recrystallised region, highlighting the development of new, small grains at the initial high-angle grain boundaries (HAGB) and triple points. This grain formation is indicative of dynamic recrystallisation, a process that occurs when the material is subjected to sufficient strain. The presence of low-angle boundaries (LAGBs) near certain initial grain boundaries (IGBs) further suggests that strain concentration was particularly pronounced in these areas.

One of the key aspects of the pore recovery mechanism involves discontinuous dynamic recrystallisation (DDRX), as evidenced by the bulging of serrated grain boundaries shown in Figure 13(d). DDRX is a faster recrystallisation process compared to continuous dynamic recrystallisation (CDRX), operating through a nucleation and growth mechanism [57]. Nucleation primarily occurs once a critical strain is reached, causing the microstructure to evolve under continued strain. The reduction of pore areas in this experimental condition was mainly achieved through enhanced plastic deformation at 1800°C, which also led to significant movement of the TZM/NbZr1 bimetal interface, as shown in the OM images (Figure 5(j–l)), demonstrating the direction of material flow. The microstructure also revealed the nucleation of new strain-free recrystallised

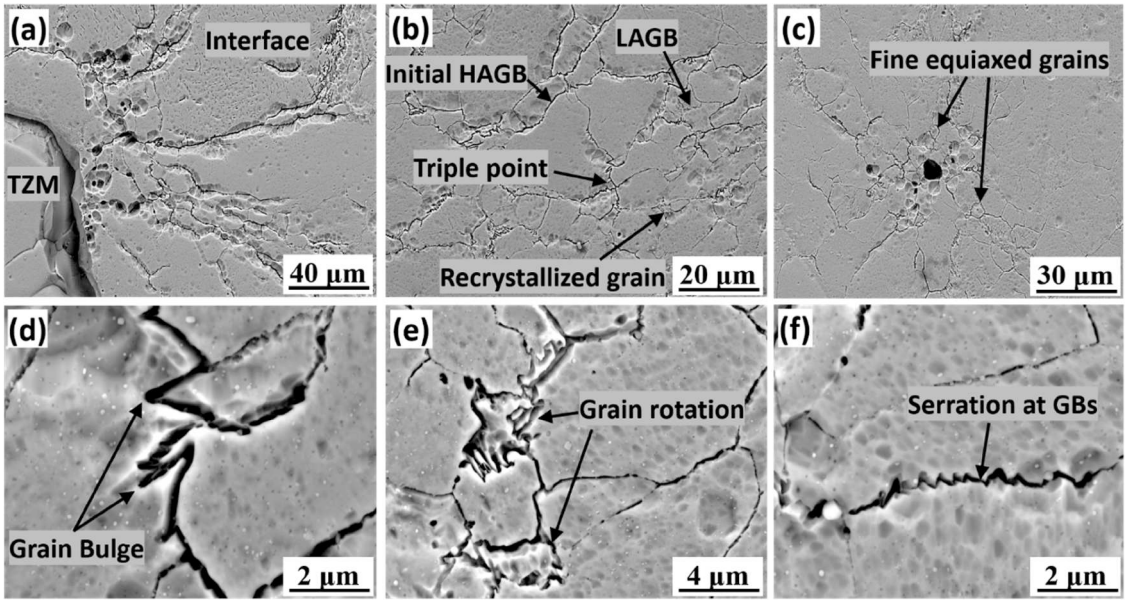

Figure 13. SEM images of (a)TZM/NbZr1 bimetallic interface after HIP-3, (b) recovered pore area with initial HAGB and recrystallised grains, (c) partially recovered pore location with recrystallised grains, (d) bulging grain boundaries at the recovered site, (e) rotation of grains, and (f) grain boundary serrations.

grains, driven by strain-induced grain boundary migration. During the HIP process, grain rotation occurs, which can be accompanied by shearing, contributing to local changes in orientation and the development of strain gradients [58]. Grain boundary shape fluctuations also occur due to grain incompatibilities, hindering further grain boundary sliding or shearing. This results in the accumulation of dislocations, leading to high dislocation density gradients and the formation of sub-grains near the original grain boundaries. The formation of dynamic recrystallisation (DRX) nuclei is facilitated by the bulging of serrated grain boundaries, which is assisted by additional inhomogeneous strain as the HIP process progresses [59]. While sub-grain formation is usually associated with CDRX processes, it is crucial for providing the driving force needed for local grain boundary migration during DDRX. This sub-grain formation near the initial grain boundary plays a vital role in the recrystallisation process [60]. Although CDRX typically occurs in materials with high stacking fault energy (SFE) [61], such as in pure Nb, the presence of serrated grain boundaries as shown in Figure 13(f) suggests that the onset of DDRX was primarily driven by strain-induced grain boundary motion (SIBM). The stored energy difference across the initial HAGB initiates local boundary migration, and when these migrating boundaries are anchored by small volumes within the microstructure, such as sub-grains, a grain boundary bulge develops [62]. The successful development of these small volumes into new grains requires a high angle of misorientation, which is provided by the HAGBs. Additionally, the bulging of parts of the HAGBs facilitates a local change in misorientation, further driving the recrystallisation process. The classical theory of SIBM, as proposed by Beck and Sperry [63], confirms this mechanism, involving the bulging of a portion of pre-existing HAGBs associated with a sub-grain. DDRX was also reported to be present during numerous hot deformation conditions of NbZr1-0.1C alloy [64].

Figure 14 shows a schematic representation of the pore recovery mechanism under HIP-3 treatment which combines HIP and HT. Figure 14(a–d) depict the progression of the pore recovery process up to the end of the isothermal stages of HIP cycle. In Figure 14 (a), the initial stage of HIP is shown where an increase in pressure induced higher strain conditions, indicating the onset of deformation. As deformation continues, there is reduction in pore surface area, leading to irregular pore shapes. Additionally, bulging of the grain boundary is observed when critical strain conditions were reached as indicated in Figure 14(b). These bulged sites served as nuclei for the development of new strain-free grains. Figure 14(c) illustrates further deformation of the pore surface with constant pressure. By the end of the isothermal stage, almost all pore areas are closed due to the combined effect of plastic deformation and dynamic recrystallisation. The red dotted regions in Figure 14(c) and (d) represent the newly formed recrystallised grains.

It is evident from the experimental results that the HIP-3 (combined HIP + HT) is effective for pore reduction

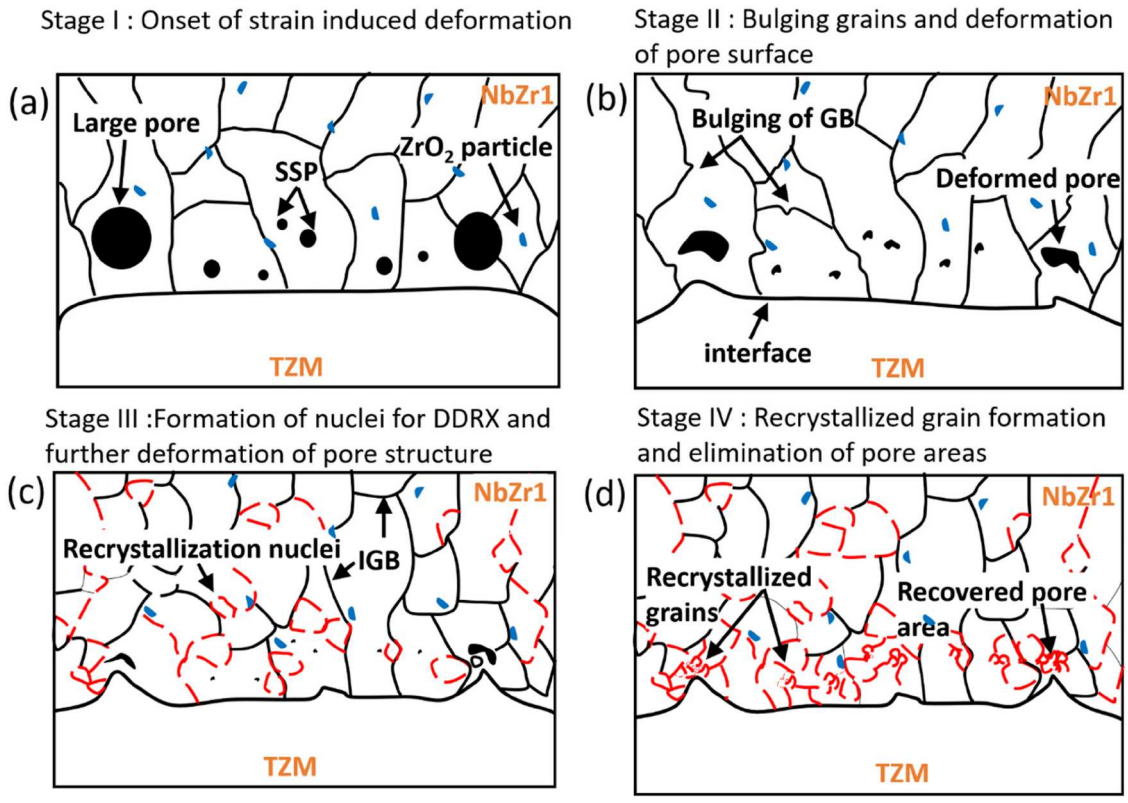

Figure 14. Schematic of pore recovery mechanism for HIP-3; (a) Initial stage of pressure development, (b) change in pore area and grain boundary bulging, (c) introduction of new recrystallised grain boundary accompanied by change in grain orientation, and (d) final structure at the end of isothermal stage of HIP.

as the recovery relies on reduced flow stress and increased plasticity. This condition has not only eliminated pores but also imparted microstructural homogeneity with fine and equiaxed recrystallised grains. Additionally, a more uniform distribution of ZrO_2 particles were attained through the subsequent HT process (Figure 10). In contrast, HIP treatments at 1200°C and 1500°C have resulted in the generation of different types of defects, including micro-cracks and micro-voids in the microstructure. However, no indication of phase transformation was evident in the microstructure with all experimented treatments, except for the dissolution of FCC carbide phases into the BCC matrix at around 1550°C, as confirmed by thermodynamic phase calculations (Figure 2). This dissolution suggests a retention of the thermo-physical properties of the initial BCC phases, minimising variations and avoiding phase separation.

4. Conclusions

In this study, different HIP treatment conditions were utilised to effectively reduce porosity from TZM-NbZr1 bimetal interface. Based on the experimental results, the key findings are summarised below:

1. In the as-built condition, the observed pore area fraction was $4 \pm 0.05\%$, with pore diameters reaching up to 720 µm. HIP treatment at 1200°C, resulted in porosity levels of $3.05 \pm 0.02\%$. Interconnected cracks were identified after HIP-1, originating from the pre-existing WAAM-induced crack.
2. HIP treatment at 1500°C (HIP-2), which is above the recrystallisation temperature of both alloys, significantly reduced porosity level to $1 \pm 0.01\%$ with the largest pore size dropping to 360 µm. However, the presence of micro-voids around the recovered pore area suggested discrepancies between material flow and applied pressure.
3. Porosity level was reduced close to $0.01 \pm 0.005\%$ after the HIP treatment at 1800°C and subsequent HT (99.75% pore reduction).
4. Increasing the HIP temperature led to increased diffusion of Mo in the NbZr1 side, and the subsequent heat treatment process effectively reduced compositional variability across the interface. No phase transformations were detected under HIP-1 and HIP-2 conditions. However, after HIP-3, the formation of secondary phases, including various oxides and carbides such as NbC, NbO, and MoO_3, was observed.

5. The pore recovery mechanism shifted from microvoid formation at the interface in HIP-2 to increased plastic deformation accompanied by dynamic recrystallisation in HIP-3.

This comprehensive investigation highlights the crucial role of HIP treatments in optimising the microstructure of TZM/NbZr1 BS. The observed transformations in pore characteristics, pore recovery mechanisms, and diffusion behaviour could contribute to a deeper understanding of the thermal processing effects on the bimetal structure, paving the way for enhanced material performance and reliability. For the development and execution of any type of material combination, the interconnected concepts of process, structure, property, and performance (PSPP) are critical. While a previous study on this bimetal combination explored the intrinsic characteristics of the deposition process and their impact on the microstructure, this study focuses on producing a more homogenous and defect-free interfacial microstructure. Our future work will focus on evaluating the structure's significant thermal and mechanical properties including creep and fatigue behaviour.

Acknowledgements

Authors of this paper acknowledge the Center for Manufacturing Research (CMR) and Tennessee Technological University's Department of Manufacturing and Engineering Technology for their support. We are grateful to Quintus Technologies LLC, in particular to Mr. Chad Beamer and Mr. Andrew Cassese, for their valuable cooperation with the HIP experiment.

Disclosure statement

No potential conflict of interest was reported by the author(s).

Funding

This material is based upon work supported by the National Science Foundation under Grant No. 2141905 and the National Research Foundation of Korea under Grant No. NRF-2021R1A2C2014025.

Data availability statement

Authors agree to make data and materials supporting the results or analyses presented in their paper available upon reasonable request.

References

[1] Knabl W, Leichtfried G, Stickler R. Refractory metals and refractory metal alloys. In: H Warlimont, W Martienssen, editor. *Springer handbook of materials data*. Cham: Springer International Publishing; 2018. p. 307–337.

[2] Islam S, Ul Ahsan MR, Seo G-J, et al. Investigations of microstructure and mechanical properties in wire + arc additively manufactured niobium–zirconium alloy. Adv Eng Mater. 2023;25:2201633. doi:10.1002/adem.202201633.

[3] Islam S, Seo GJ, Ahsan MRU, et al. Investigation of microstructures, defects, and mechanical properties of titanium-zirconium-molybdenum alloy manufactured by wire arc additive manufacturing. IInt J Refract Met Hard Mater. 2023;110(November 2022):106042. doi:10.1016/j.ijrmhm.2022.106042

[4] Zhang C, Peng Y, Zhou P, et al. Thermodynamic assessment of the C–Nb–Mo system over the entire composition and temperature ranges. Calphad. 2015;51:104–110. doi:10.1016/j.calphad.2015.09.001

[5] Yang ZW, Sun KB, Lin JM, et al. Microstructure and mechanical properties of contact-reactive brazed TZM/Nb-Zr joints with Ni interlayer. J Manuf Process. 2020;57:817–827. doi:10.1016/j.jmapro.2020.07.042

[6] Lin JM, Yang ZW, Wei HH, et al. An investigation on diffusion bonding of TZM alloy and Nb-Zr alloy using Ni foil as an interlayer. J Alloys Compd. 2018;743:780–788. doi:10.1016/j.jallcom.2018.01.162

[7] Yang ZW, Lin JM, Zhang JF, et al. An effective approach for bonding of TZM and Nb-Zr system: Microstructure evolution, mechanical properties, and bonding mechanism. J Mater Sci Technol. 2021;84:16–26. doi:10.1016/j.jmst.2020.09.054

[8] Ahsan MRU, Tanvir ANM, Ross T, et al. Fabrication of bimetallic additively manufactured structure (BAMS) of low carbon steel and 316L austenitic stainless steel with wire + arc additive manufacturing. Rapid Prototyp J. 2020;26(3):519–530. doi:10.1108/RPJ-09-2018-0235

[9] Karim MA, Jadhav S, Kannan R, et al. Investigating stainless steel/aluminum bimetallic structures fabricated by cold metal transfer (CMT)-based wire-arc directed energy deposition. Addit Manuf. 2024;81:104015. doi:10.1016/j.addma.2024.104015

[10] Treutler K, Wesling V. The current state of research of wire arc additive manufacturing (WAAM): a review. Appl Sci. 2021;11(18):8619. doi:10.3390/app11188619

[11] Tan C, Li R, Su J, et al. Review on field assisted metal additive manufacturing. Int J Mach Tools Manuf. 2023;189:104032. doi:10.1016/j.ijmachtools.2023.104032

[12] Zahidin MR, Yusof F, Hanim S, et al. Research challenges, quality control and monitoring strategy for wire arc additive manufacturing. J Mater Res Technol. 2023;24:2769–2794. doi:10.1016/j.jmrt.2023.03.200

[13] Jadhav S, Karim MA, Kim DB. Bimetallic structure of TZM and NbZr1 fabricated by wire-based directed energy deposition. Mater Lett. 2023;356:135605. doi:10.1016/j.matlet.2023.135605

[14] Kubaschewski O, Hopkins BE. Oxidation mechanisms of niobium, tantalum, molybdenum and tungsten. J Less Common Met. 1960;2(2):172–180. doi:10.1016/0022-5088(60)90012-6

[15] Cegan T, Pagac M, Jurica J, et al. Effect of hot isostatic pressing on porosity and mechanical properties of 316 L stainless steel prepared by the selective laser melting method. Materials (Basel). 2020;13(19):1–26. doi:10.3390/ma13194377

[16] du Plessis A, Macdonald E. Hot isostatic pressing in metal additive manufacturing: X-ray tomography reveals details of pore closure. Addit Manuf. 2020;34:101191. doi:10.1016/j.addma.2020.101191
[17] Guan B, Yang X, Tang J, et al. Strategies to Reduce Pores and Cracks of Molybdenum Fabricated by Selective Laser Melting. Int J Refract Met Hard Mater. 2023;112:106123. doi:10.1016/j.ijrmhm.2023.106123
[18] Kim H, Lin Y, Tseng T-LB. A review on quality control in additive manufacturing. Rapid Prototyp J. 2018;24 (3):645–669. doi:10.1108/RPJ-03-2017-0048
[19] Mclean N, Bermingham MJ, Colegrove P, et al. Effect of hot isostatic pressing and heat treatments on porosity of wire arc additive manufactured Al 2319. J Mater Process Technol. 2022;310:117769. doi:10.1016/j.jmatprotec.2022.117769
[20] Tillmann W, Schaak C, Nellesen J, et al. Hot isostatic pressing of IN718 components manufactured by selective laser melting. Addit Manuf. 2017;13:93–102. doi:10.1016/j.addma.2016.11.006
[21] Polozov I, Gracheva A, Popovich A. Interface characterization of bimetallic Ti-6Al-4 V/Ti2AlNb structures prepared by selective laser melting. Materials (Basel). 2022;15 (23):8528. doi:10.3390/ma15238528
[22] Terrazas CA, Gaytan SM, Rodriguez E, et al. Multi-material metallic structure fabrication using electron beam melting. Int J Adv Manuf Technol. 2014;71(1):33–45. doi:10.1007/s00170-013-5449-0
[23] Bernal D, Chamorro X, Hurtado I, et al. Integration of hot isostatic pressing and heat treatment for advanced modified γ-TiAl TNM alloys. Materials (Basel). 2022;15 (12):4211. doi:10.3390/ma15124211
[24] Chadha K, Tian Y, Spray JG, et al. Effect of Annealing Heat Treatment on the Microstructural evolution and mechanical properties of hot isostatic pressed 316L stainless steel fabricated by laser powder bed fusion. Metals (Basel). 2020;10(6):1–18. doi:10.3390/met10060753
[25] Hafenstein S, Brummer M, Ahlfors M, et al. Combined hot isostatic pressing and heat treatment of aluminum A356 cast alloys. HTM J Heat Treat Mater. 2016;71(3):117–124. doi:doi:10.3139105.110281.
[26] Chen J, Li K, Wang Y, et al. The effect of hot isostatic pressing on thermal conductivity of additively manufactured pure tungsten. IInt J Refract Met Hard Mater. 2020;87:105135. doi:10.1016/j.ijrmhm.2019.105135
[27] Danisman CB, Yavas B, Yucel O, et al. Processing and characterization of spark plasma sintered TZM alloy. J Alloys Compd. 2016;685:860–868. doi:10.1016/j.jallcom.2016.06.161
[28] Atkinson HV, Davies S. Fundamental aspects of hot isostatic pressing: an overview. Metall Mater Trans A. 2000;31(12):2981–3000. doi:10.1007/s11661-000-0078-2
[29] Cockeram BV, Smith RW, Snead LL. The influence of fast neutron irradiation and irradiation temperature on the tensile properties of wrought LCAC and TZM molybdenum. J Nucl Mater. 2005;346(2):145–164. doi:10.1016/j.jnucmat.2005.06.016
[30] Begley RT, Bechtold JH. Effect of alloying on the mechanical properties of niobium. J Less Common Met. 1961;3 (1):1–12. doi:10.1016/0022-5088(61)90037-6
[31] Siciliano F, Monteiro W, Padilha A. Comparative Study of the Recrystallization of Pure Niobium and a Nb-1 Wt.% Zr Alloy. Int J Mater Res. 1995;86(October):713–718.
[32] Kar SK, Voramon SD, Don ML Phase stability in the Mo-Ti-Zr-C system via thermodynamic modeling and diffusion multiple validation. Metall Mater Trans A-Phys Metall Mater Sci. 2013;44(8):3999–4010. doi:10.1007/s11661-013-1705-z
[33] Garcia JC, Scolfaro LMR, Lino AT, et al. Structural, electronic, and optical properties of ZrO2 from Ab initio calculations. J Appl Phys. 2006;100(10):104103. doi:10.1063/1.2386967
[34] Rodrigues TA, Duarte V, Miranda RM, Santos TG, Oliveira JP. Current status and perspectives on wire and arc additive manufacturing (WAAM). Mater. 2019;12(7):1121. doi:10.3390/ma12071121
[35] Causey RA, Donald FC, Robert HN. Review of the oxidation rate of zirconium alloys. Sandia Report, SAND2005-6006, United States. 2005. doi: 10.2172/876346
[36] Xu Q, Li W, Yin Y, et al. Effect of hot isostatic pressing on the cast Ti6Al4V alloy with shrinkage cavities inside: healing behavior, microstructure evolution and tensile property. Mater Sci Eng: A. 2022;832:142496. doi:10.1016/j.msea.2021.142496
[37] Gurmesa FD, Lemu HG. Literature review on thermo-mechanical modelling and analysis of residual stress effects in wire arc additive manufacturing. Metals (Basel). 2023;13(3):526. doi:10.3390/met13030526
[38] Fan K, Wang GZ, Xuan FZ, et al. Effects of work hardening mismatch on fracture resistance behavior of Bi-material interface regions. Mater Des. 2015;68:186–194. doi:10.1016/j.matdes.2014.12.031
[39] Okamoto H. Mo-Nb (molybdenum-niobium). J Ph Equilibria. 1991;12(5):616–617. doi:10.1007/BF02645086
[40] Zhang H, Yong D, Zhuoyue S, Peng Z, Yingbiao P, Shuhong L, Yi K, Rajkumar VB. Thermodynamic modeling and solidified microstructure in the Mo–Nb–Zr ternary system. Calphad. 2019;66:101630. doi:10.1016/j.calphad.2019.101630
[41] Zhang H, Cong Z, Peng Z, Yong D, Yingbiao P, Shuhong L, Jiong W, Kun L. Experimental investigation of the Mo–Ti–Zr ternary phase diagrams. JPED. 2018;39 (6):789–799. doi:10.1007/s11669-018-0668-6
[42] Ng CH, Bermingham MJ, Kent D, et al. High stability and high strength β-titanium alloys for additive manufacturing. Mater Sci Eng: A. 2021;816:141326. doi:10.1016/j.msea.2021.141326
[43] Storms EK, Krikorian NH. The niobium—niobium carbide system. J Phys Chem. 1960;64(10):1471–1477. doi:10.1021/j100839a029
[44] Vishwanadh B, Arya A, Tewari R, et al. Formation mechanism of stable NbC carbide phase in Nb-1Zr-0.1C (Wt.%) alloy. Acta Mater. 2018;144:470–483. doi:10.1016/j.actamat.2017.11.007
[45] Ghaemifar S, Mirzadeh H. Precipitation Kinetics of Niobium Carbide (NbC) during Homogenization Heat Treatment of Additively Manufactured Inconel 718 Superalloy. J Mater Res Technol. 2023;25:1774–1781. doi:10.1016/j.jmrt.2023.06.069
[46] Viswanadham RK, Wert CA. Electron microscopic study of precipitation in the system niobium-carbon. J Less Common Met. 1976;48(1):135–150. doi:10.1016/0022-5088(76)90239-3
[47] DiStefano JR, Chitwood LD. Oxidation and its effects on the mechanical properties of Nb-1Zr. J Nucl Mater. 2001;295 (May):42–48. doi:10.1016/S0022-3115(01)00495-0

[48] Fridriksson EG, Tryggvason TK, Arnalds UB, et al. Growth of NbO, NbO2 and Nb2O5 thin films by reactive magnetron sputtering and post-annealing. Vacuum. 2022;202:111179. doi:10.1016/j.vacuum.2022.111179
[49] Nico C, Monteiro T, Graça MPF. Niobium oxides and niobates physical properties: review and prospects. Prog Mater Sci. 2016;80:1–37. doi:10.1016/j.pmatsci.2016.02.001
[50] Puebla S, D'Agosta R, Sanchez-Santolino G, et al. In-Plane Anisotropic Optical and Mechanical Properties of Two-Dimensional MoO3. Npj 2D Mater Appl. 2021;5(1):37. doi:10.1038/s41699-021-00220-5
[51] Liu Y, Long Z, Du Y, et al. Diffusion characteristics and atomic mobilities for Bcc refractory Mo–Ta, Mo–W, and Mo–Nb alloys. Calphad. 2012;36:110–117. doi:10.1016/j.calphad.2011.12.004
[52] Kingery WD, Woulbroun JM, Charvat FR. Effects of applied pressure on densification during sintering in the presence of a liquid phase. J Am Ceram Soc. 1963;46(8):391–395. doi:10.1111/j.1151-2916.1963.tb11758.x
[53] Irukuvarghula S, Hassanin H, Cayron C, et al. Evolution of grain boundary network topology in 316L austenitic stainless steel during powder hot isostatic pressing. Acta Mater. 2017;133:269–281. doi:10.1016/j.actamat.2017.04.068
[54] Prasad MRG, Gao S, Vajragupta N, et al. Influence of trapped gas on pore healing under hot isostatic pressing in nickel-base superalloys. Crystals (Basel). 2020;10(12):1–15. doi:10.3390/cryst10121147
[55] Dekhtyar AI, Bondarchuk VI, Nevdacha VV, et al. The effect of microstructure on porosity healing mechanism of powder near-β titanium alloys under hot isostatic pressing in α + β-region: Ti-10V-2Fe-3Al. Mater Charact. 2020;165:110393. doi:10.1016/j.matchar.2020.110393.
[56] Li P, Warner DH, Pegues JW, Roach MD, Shamsaei N, Phan N. Investigation of the mechanisms by which hot isostatic pressing improves the fatigue performance of powder bed fused Ti-6Al-4V. Int J Fatigue. 2019;120:342–352. doi:10.1016/j.ijfatigue.2018.10.015
[57] Sakai T, Andrey B, Rustam K, Hiromi M, John JJ. Dynamic and post-dynamic recrystallization under hot, cold and severe plastic deformation conditions. Prog Mater Sci. 2014;60:130–207. doi:10.1016/j.pmatsci.2013.09.002
[58] Liu J, Huiqin C. Nucleation and grain boundary evolution in dynamic recrystallization of 316LN steel during hot deformation. Front Mater. 2019;6:209. doi:10.3389/fmats.2019.00209
[59] Huang K, Logé RE. A review of dynamic recrystallization phenomena in metallic materials. Mater Des. 2016;111:548–574. doi:10.1016/j.matdes.2016.09.012
[60] Momeni A, Ebrahimi GR, Jahazi M, Bocher P. Microstructure evolution at the onset of discontinuous dynamic recrystallization: a physics-based model of subgrain critical size. J Alloys Compd. 2014;587:199–210. doi:10.1016/j.jallcom.2013.10.180
[61] Park SY, Woo JK. Microstructural and texture evolution in pure niobium during severe plastic deformation by differential speed rolling. J Mater Res and tech. 2022;22:2704-2719. doi:10.3390/ma15030752
[62] Sun DK, Chang CP, Kao PW. Microstructural aspects of grain boundary bulge in a dynamically recrystallized Mg-Al-Zn alloy. MMTA. 2010;41(7):1864–1870. doi:10.1007/s11661-010-0220-8
[63] Beck PA, Philip RS. Strain induced grain boundary migration in high purity aluminum. J Appl Phys. 1950;21(2):150–152. doi:10.1063/1.1699614
[64] Chaudhuri A, Apu S, Rajeev K, Ram NS, Jayanta KC, Satyam S. Microstructural features of hot deformed Nb-1Zr-0.1C alloy. JOM. 2014;66(9):1923–1929. doi:10.1007/s11837-014-1122-9